

Article

Simulation of Fluid Flow in the Top–Bottom Combined Blowing Converter

Zhao Liu, Shusen Cheng * and Jipeng Peng

School of Metallurgical and Ecological Engineering, University of Science and Technology Beijing, Xueyuan Road 30, Beijing 100083, China; liuzhaoheuu@163.com (Z.L.); 18610292294@163.com (J.P.)

* Correspondence: chengsusen@metall.ustb.edu.cn; Tel.: +86-10-6233-2265

Abstract: The flow in the top–bottom combined blowing converter has an important impact on processes such as slagging, dephosphorization, decarburization, the heating of molten steel, and the homogenization of steel composition and temperature. A 1/6 reduced scale model based on a 210 t converter was used for the mathematical simulation. The validity of the model was verified by comparing the variation in cavity sizes caused by changes in the lance height and flow rate of the physical model with the numerical results. It was found that, in the bottom blowing converter, the area with higher velocity was distributed in the inverted conical plume. In top blowing, the area with higher velocity was distributed on the surface of a molten bath. The area of higher molten bath velocity in the combined blowing converter further increased. Compared with the top blowing converter, the increased percentage of the area-averaged velocity in the combined blowing converter first increased and then decreased as the distance from the bottom increased. When the top blowing flow rate changed, the combined blowing made the velocity change at the top of a molten bath smaller. The decrease in lance height significantly reduced the ratio of “inactive zone”, while the effect of the change in the flow rate was slight.

Keywords: converter; flow field; combined blowing; physical model; numerical simulation



Citation: Liu, Z.; Cheng, S.; Peng, J. Simulation of Fluid Flow in the Top–Bottom Combined Blowing Converter. *Metals* **2024**, *14*, 56. <https://doi.org/10.3390/met14010056>

Academic Editor: Marta Oliveira

Received: 2 November 2023

Revised: 23 December 2023

Accepted: 27 December 2023

Published: 3 January 2024



Copyright: © 2024 by the authors. Licensee MDPI, Basel, Switzerland. This article is an open access article distributed under the terms and conditions of the Creative Commons Attribution (CC BY) license (<https://creativecommons.org/licenses/by/4.0/>).

1. Introduction

At present, top and bottom combined blowing is the most dominant method of steelmaking in the converter [1]. The interaction between the top-blown oxygen jet and the bottom-blown gas significantly affects the kinetic behavior of the converter bath. Since computational fluid dynamics (CFDs) models can provide better insight into melt flow-related phenomena and make the BOF process more transparent, many researchers use CFDs to study the converter blowing process. Alam [2] developed a VOF model to simulate the liquid flow field and surface deformation and found that, the larger the gas flow rate, the bigger the penetration depth, as well as the smaller the mixing time. Lv et al. [3] simulated the effect of oxygen flow, lance height, and slag thickness on the flow of a molten bath in a top-blown converter. The results showed that the impact area increases with the increase in lance height, which is beneficial to the uniform distribution of the radial velocity of a molten bath and increases the flow velocity of molten steel at the bottom of the furnace hearth. Li et al. [4] reported that the penetration depth increases with the decline in lance height, while the impact area decreases. However, the impact area is almost unaffected by the operating pressure. Zhou et al. [5] developed a mathematical model of a top-blown converter and found that the cavity depth and radius obtained were close to the physical model. Li et al. [6] reported that, compared to the viscosity and surface tension of the melts, the operating pressure and lance height have a much more significant impact on the slag–metal interface behavior and cavity shape, as well as the fluid dynamics in a molten bath. Zhou and Ersson et al. [7] found that the energy transfer for the bottom blowing is much more efficient than that of the top blowing operations. Liu et al. [8] found

that more than 75% of the total energy is wasted in the process of jet attenuation, and the energy used for stirring the bath is less than 1.5% of the total energy. Li et al. [9] presented a numerical study of transferring the characteristics of momentum/energy during oxygen jetting into the slag–metal molten bath. The results showed that decreasing the lance height or increasing the operation pressure promotes the efficiency of the momentum transfer from the jets to a molten bath but lowers the efficiency of the kinetic energy transfer. In addition, by considering the flow fields and the “inactive zone” volume for the bath, bottom blowing dominates the flow or stirring during combined blowing for the current operations [10]. Ajmani et al. [11] used a cold model to simulate a combined-blown converter and top-blown converter. The results indicated that the mixing time is highest with pure top blowing, and the mixing is improved markedly by an injection of even a small amount of gas from the bottom. Liu et al. [12] recognized that, in the initial stage of the interaction, the low stirring zone in a molten bath is more likely to deviate from the central of the converter. Li et al. [13] developed a theoretical model to predict the cavity depth of a two-layer liquid bath impinged by multiple gas jets. Amano et al. [14] used a water model experiment and numerical simulation to show that interference between the top-blown gas jet and the bottom-blowing plume can increase the spitting rate. Sun et al. [15–17] used the VOF (volume of fluid) model to numerically study the behavior of a supersonic jet impinging on a molten steel bath in a 100 t converter. The results showed that the lance height has a larger influence on altering the cavity dimensions. For the bottom blowing, arranging the tuyeres in the corner region of scattered cavities would exacerbate the nonuniformity of the velocity and splashing, resulting in a large dead zone and high kinetic energy dissipation, which is not favorable to the mixing of a molten bath. Qi et al. [18] developed a three-dimensional (3D) transient mathematical model coupled with CLSVOF method to analyze the mixing process under different injection flow rates and bottom blowing positions. The findings indicate that managing the bottom blowing flow rate is an essential aspect of optimizing the converter performance. Zhang et al. [19] studied the two-phase flow in a top–bottom combined-blown converter and found that the drag force powerfully influences the impact cavity shape, while the turbulent dispersion force has less influence, but it dominates the bottom blowing flow direction.

In this work, based on actual steelmaking conditions, three lance heights and three oxygen flow rates were used to study the morphology of the cavity and flow characteristics of a molten bath. A detailed comparison was performed to elucidate the flow characteristics of a molten bath within bottom, top, and combined blowing converters. Furthermore, the influence of the operating parameters on the “inactive zone” of a molten bath is also explored.

2. Physical Model

Based on the 210 t converter of a steel plant in China, a 1/6 reduced scale model was made, which was made of plexiglass. The physical model was conducted on the basis of Figure 1. In the experiment, water, oil, and air were used to represent liquid steel, liquid slag, and argon, respectively. The air was supplied by a compressor that pumped the air into a gas container. The air flow rate was controlled by rotameters. Six bottom tuyeres were arranged on a 0.5 D (D is the diameter of the molten bath). A video camera was used to record the cavity contours and dimensions during the experiment.

According to the similarity principle, the modified Froude criterion number was applied as the main similarity criterion to assure the fluid motion similarity of the real system and model [20,21].

$$Fr'_W = Fr'_P \quad (1)$$

$$\frac{u_W^2}{gL_W} \cdot \frac{\rho_{gW}}{\rho_{lW} - \rho_{gW}} = \frac{u_P^2}{gL_P} \cdot \frac{\rho_{gP}}{\rho_{lP} - \rho_{gP}} \quad (2)$$

$$Q = u \times n \times \frac{\pi}{4} \times L^2 \times 3600 \quad (3)$$

$$\frac{Q_W}{Q_P} = \left(\frac{L_W}{L_P}\right)^{5/2} \times \left(\frac{\rho_{gP}}{\rho_{gW}}\right)^{1/2} \times \left(\frac{\rho_{lW} - \rho_{gW}}{\rho_{lP} - \rho_{gP}}\right)^{1/2} \quad (4)$$

$$\frac{Q_W}{Q_P} = \left(\frac{L_W}{L_P}\right)^{5/2} \times \left(\frac{\rho_{gP}}{\rho_{gW}}\right)^{1/2} \times \left(\frac{\rho_{lW}}{\rho_{lP}}\right)^{1/2} \quad (5)$$

where subscripts P and W represent the parameters of the prototype and water model, respectively; u is the velocity of the gas (m/s); ρ_g is the density of the gas (kg/m³); ρ_l is the density of the liquid (kg/m³); Q is the gas flow rate (m³/h); n is the number of nozzles; L is the liquid; and g is the gas. Because the density of the liquid is much higher than that of the gas, the third term on the right-hand side of Equation (4) ignores the density of the gas, and Equation (5) can be obtained. The main parameters of the converter and oxygen lance are listed in Table 1. The diameter and depth of the molten bath are 1/6 of the prototype, and the size and height of the oxygen lance are also 1/6 of the prototype. In the model, three bottom blowing flow rates of 1.96 m³/h, 3.92 m³/h, and 5.88 m³/h were selected. Three kinds of lance heights were selected: 0.266 m, 0.333 m, and 0.400 m respectively, and the three kinds of top blowing flows were 203.38 m³/h, 221.87 m³/h, and 240.36 m³/h, respectively.

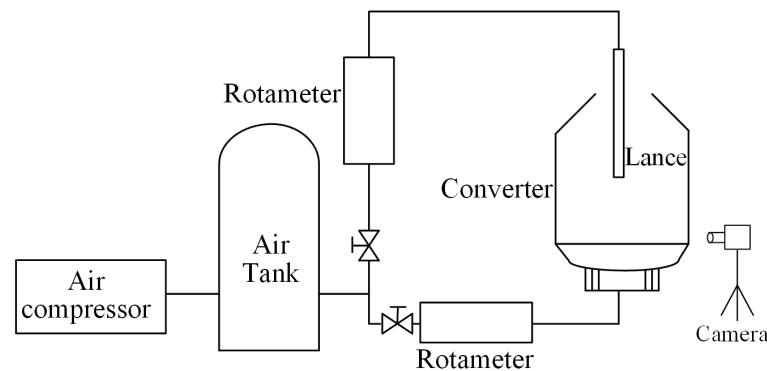


Figure 1. Schematic diagram of the experimental apparatus.

Table 1. Parameters of the converter and oxygen lance.

	Parameter	Prototype	Model
Converter	Converter capacity (t)	210	-
	Similarity ratio	6	1
	Bath diameter (mm)	5600	933
	Bath depth (mm)	1630	271
	Bottom flow rate (m ³ /h)	400, 800, 1200	1.96, 3.92, 5.88
Lance	Nozzles	5	5
	Inclination angle (°)	15.5	15.5
	Throat diameter (mm)	45.2	7.5
	Exit diameter (mm)	59.5	9.9
	Lance height (m)	1.6, 2.0, 2.4	0.266, 0.333, 0.400
	Flow rate (m ³ /h)	44,000, 48,000, 52,000	203.38, 221.87, 240.36

3. Mathematical Model

3.1. Assumption

Since the phenomena in the converter are very complex, the mathematical model of the fluid flow is based on the following assumptions:

(1) The wall of the converter was regarded as non-slip, and the velocity distribution near the wall was calculated by the standard wall function.

(2) Water, oil, slag, and steel were regarded as Newtonian fluids, and the other fluid physical parameters were constants.

(3) The surface tension of all the phases was considered as constant during the numerical simulation.

(4) The influence of chemical reactions on the flow in the converter was ignored.

3.2. VOF Model

The volume of fluid (VOF) model can simulate two or more immiscible fluids by solving individual momentum equations and processing the volume fraction of each phase passing through the entire region [19,22].

The calculation of the volume fraction of the primary phase was based on the following equation:

$$\sum_{i=1}^n \alpha_i = 1 \quad (6)$$

All variable properties that appeared in the transport equation were determined by each phase, and the equations were expressed as

$$\rho = \sum_{i=1}^n \alpha_i \rho_i \quad (7)$$

$$\mu = \sum_{i=1}^n \alpha_i \mu_i \quad (8)$$

where ρ is the average density of the volume fraction ($\text{kg}\cdot\text{m}^{-3}$); α_i is the i th volume fraction; ρ_i is the density of the i th phase ($\text{kg}\cdot\text{m}^{-3}$); for the gas, the phase satisfies the ideal gas state equation, i.e., $p = \rho RT$, p is the pressure (MPa), R is the gas constant, and T is the temperature (K); for the liquid, the density is considered to be constant; μ is the average viscosity of the volume fraction, ($\text{kg}\cdot\text{m}^{-1}\cdot\text{s}^{-1}$); and μ_i is the viscosity of the i th phase, ($\text{kg}\cdot\text{m}^{-1}\cdot\text{s}^{-1}$).

In the VOF model, the entire amount of fluid is regarded as a one-phase flow. Thus, a single set of momentum equations was solved. The resulting velocity field was shared by all phases. The momentum equation is shown as follows:

$$\frac{\partial}{\partial t}(\rho \vec{v}) + \nabla \times (\rho \vec{v} \vec{v}) = -\nabla p + \nabla \times [\mu(\nabla \vec{v} + \nabla \vec{v}^T)] + \rho \vec{g} + \vec{F} \quad (9)$$

where ρ and μ are provided in Equations (7) and (8); \vec{v} is the instantaneous velocity of the phase ($\text{m}\cdot\text{s}^{-1}$); g is the gravity acceleration ($\text{m}\cdot\text{s}^{-2}$); and \vec{F} is the volume force ($\text{kg}\cdot\text{m}^{-2}\cdot\text{s}^{-2}$).

In the VOF method, all variables are calculated based on Reynolds averaged Navier–Stokes equations. Among them, the continuity equation and the energy conservation equation are shown in Equations (10) and (11), respectively.

$$\frac{\partial \rho}{\partial t} + \nabla \cdot (\rho \vec{u}) = 0 \quad (10)$$

$$\frac{\partial(\rho E)}{\partial t} + \nabla \cdot [\vec{u}(\rho E + P)] = \nabla \cdot (\lambda_{eff} \nabla T) + S_h \quad (11)$$

where \vec{u} is the velocity vector of the fluid ($\text{m}\cdot\text{s}^{-1}$); P is the static pressure of the fluid (MPa); E is energy as a mass-averaged variable (J); λ_{eff} is the effective thermal conductivity ($\text{W}\cdot\text{m}^{-1}\cdot\text{K}^{-1}$); and S_h is the volumetric heat sources ($\text{W}\cdot\text{m}^{-1}$).

3.3. Turbulence Models

The standard k - ε turbulent model was used to solve the flow field in the BOF. The turbulent kinetic energy k and the turbulent energy dissipation rate ε equations are as follows:

$$\frac{\partial}{\partial t}(\rho k) + \frac{\delta}{\delta x_i}(\rho k u_i) = \frac{\delta}{\delta x_j} \left[\left(\mu + \frac{\mu_t}{\sigma_k} \right) \frac{\delta k}{\delta x_j} \right] + G_k + G_b - \rho \varepsilon - Y_M + S_k \quad (12)$$

$$\frac{\partial}{\partial t}(\rho \varepsilon) + \frac{\partial}{\partial x_i}(\rho \varepsilon u_i) = \frac{\delta}{\delta x_j} \left[\left(\mu + \frac{\mu_t}{\sigma_k} \right) \frac{\delta \varepsilon}{\delta x_j} \right] + C_{1\varepsilon} \frac{\varepsilon}{k} (G_k + C_{3\varepsilon} G_b) - C_{2\varepsilon} \rho \frac{\varepsilon^2}{k} + S_\varepsilon \quad (13)$$

where G_k is the generation of the turbulence kinetic energy owing to the mean velocity gradients; G_b is the generation of turbulence kinetic energy owing to the buoyancy; Y_M is the contribution of the fluctuating dilatation in compressible turbulence to the overall dissipation rate; and $C_{1\varepsilon}$, $C_{2\varepsilon}$, $C_{3\varepsilon}$, σ_k , and σ_ε are constant and have default values [23]. S_k and S_ε are the user-defined turbulent energy phase and dissipation rate source phase, respectively.

3.4. Boundary Conditions and Solution Procedure

In order to overcome the difficulty of convergence in calculating compressible gases, Model A and Model B were developed to calculate the top blowing free jet and multiphase flow behaviors, as shown in Figure 2. The size of the Laval nozzle in Model A is the same as that in Table 1. Only model the bottom of the converter to reduce the computational complexity, as shown in Model B. The height of model B is 400 mm, and the diameter is 933 mm. A circle with a diameter of 200 mm is set above Model B as the upper inlet. At first, the oxygen lance gas jet was simulated at a cylindrical zone, in which the diameter and height were 200 mm and 300 mm, respectively. According to the different lance heights, three corresponding cross-sections are taken from model A. Then, the data of the cross-section selected in Model A, including the velocity, pressure, turbulent kinetic energy, and turbulent dissipation rate, are imported to model B as the inlet boundary conditions. The effectiveness of this method has been confirmed by researchers [5,16,17]. To reduce the computational cost, the calculated domain was simplified, and only half of the converter was simulated. A workbench was used to create Poly-Hexcore grids for models A and B with a minimum orthogonal quality of 0.65, as shown in Figure 3. Local mesh refinement was performed near the Laval nozzle and the bottom tuyere. The application of Poly-Hexcore can reduce the total element count and speed up the Fluent solver [24].

The inlet of Model A adopted the mass flow inlet boundary condition, and the outlet adopted the pressure boundary condition. Due to the high jet velocity, the initial time step of Model A was 1×10^{-6} s. Then, an adaptive method was selected. A steady state was reached after approximately 4 s. The upper inlet of Model B adopted the velocity boundary condition, which was obtained from Model A. The upper outlet was the pressure outlet boundary condition. The inlet at the bottom adopted the mass flow inlet boundary condition. The time step of Model B was 1×10^{-3} s. Thereafter, model B was used to calculate the long time conditions.

The PISO (pressure implicit with splitting of operators) algorithm was used to couple the pressure and velocity terms. The momentum and mass equation were solved with the second-order upwind method. The interpolation of the pressure values was achieved with the pressure staggering option (PRESTO!) algorithm. Geo-Reconstruct was adopted to track the free interface. In this paper, the double-precision solver was applied to minimize the rounding errors. The numerical calculations of the two models were performed with the commercial software Fluent 2022R1. When the residual of the energy equation was less than 1×10^{-6} and the other variables residuals were less than 1×10^{-3} , the calculations converged. The comparison of models A and B is shown in Table 2.

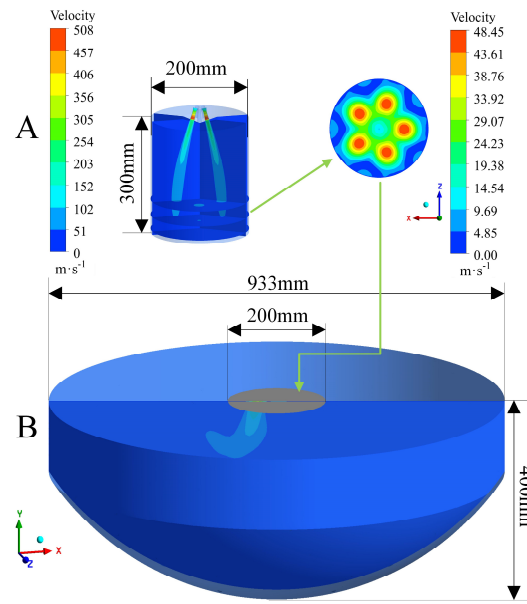


Figure 2. Schematic of the mathematical model simplification ((A) gas jet, (B) molten bath).

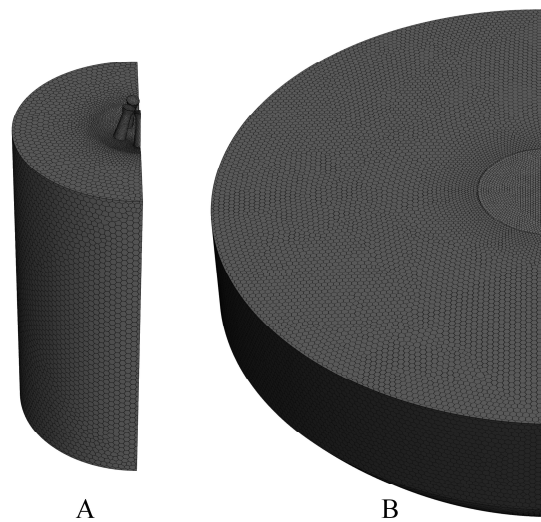


Figure 3. Diagram meshing of Modal A (single phase domain) and Modal B (multiphase domain).

Table 2. Comparison of Model A and Model B.

	Model A	Model B
inlet	mass flow inlet	upper: profile data inlet bottom: mass flow inlet
outlet	pressure outlet	pressure outlet
wall	no slip	no slip
time step	1×10^{-6}	1×10^{-3}
phase	air	air, oil, water

3.5. Mesh Sensitivity

The grid sensitivity of model A and B was analyzed. For Model A, four grid number schemes were examined, as shown in Figure 4. The results showed that the maximum error was less than 5% when the number of grids was 248,655 and 292,840. When the number of grids was 153,481 and 203,275, the number of grids had a great influence on the calculation

results. Considering the accuracy and computational efficiency of the calculation results, a scheme with a grid of 248,655 was selected for this study. For model B, three grid number schemes (142,455, 193,326, and 397,401) were used for testing. It can be seen from Figure 5 that, when the number of grids was 193,326 and 397,401, the number of grids had little effect on the calculation results, and the maximum error was less than 3%. When the number of grids was 142,455 and 193,326, the number of grids had a great influence on the calculation results. Therefore, the scheme of the 193,326 grid number was selected for this study.

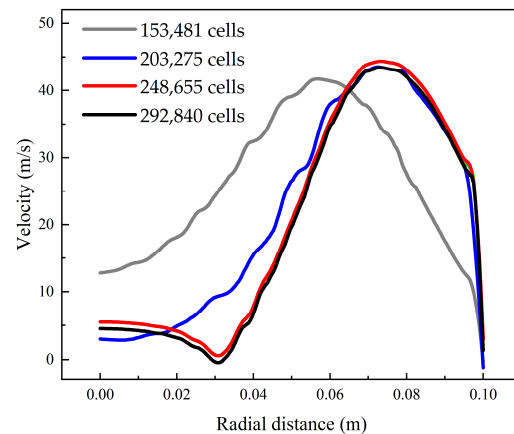


Figure 4. Radial velocity distribution at the outlet of Model A.

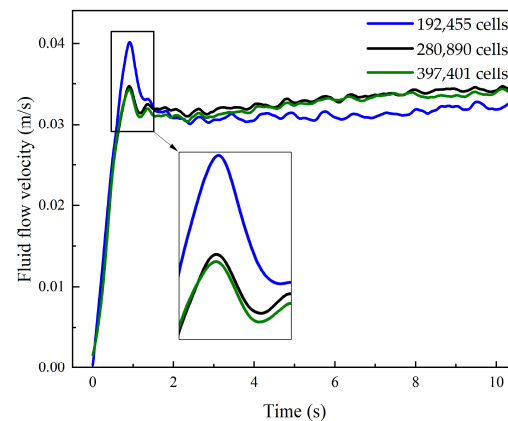


Figure 5. Fluid flow velocity of the molten bath at different grid levels.

4. Results and Discussion

4.1. The Morphology of the Impact Cavity

Figure 6 depicts the cavity morphology obtained from the water model experiments and numerical simulation. H_c represents the depth of the cavity. D_c represents the radius of the cavity.

Figure 7 reveals a comparison of the measured and simulated values of the cavity depth H_c . As the figure shows, the measured values and simulation results are relatively close. It can be concluded that the fully developed cavity is obtained after 6 s of blowing.

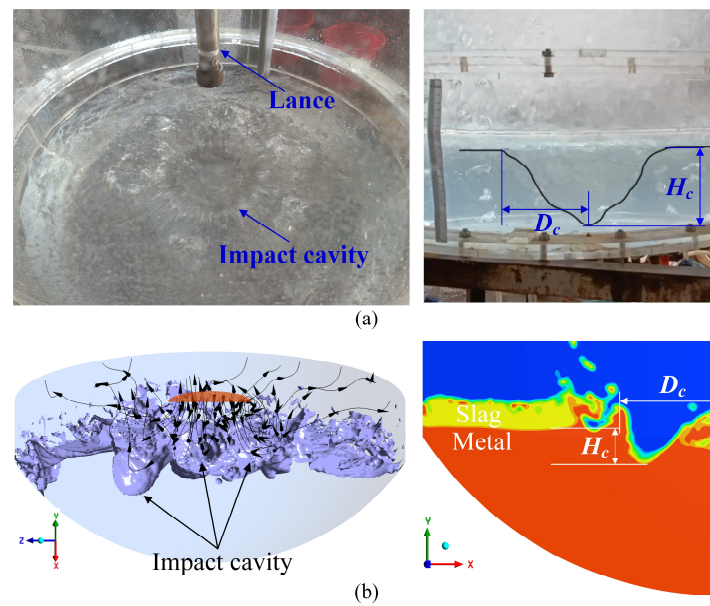


Figure 6. Cavity shape in the (a) physical model and (b) numerical simulation.

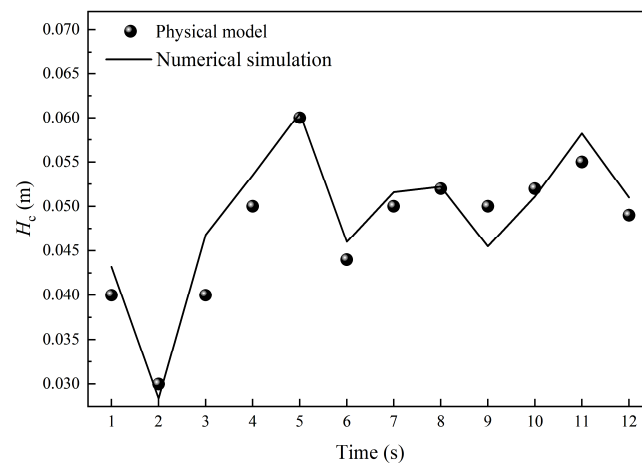


Figure 7. Variations of the cavity depth with time.

Figures 8 and 9, drawn using CFD-Post 2022R1 software, illustrate the evolution of the blowing cavities with time for the top-blown and combined-blown converters by snapshots of 0.1 s to 6.0 s. The arrows in the contour represent the direction of fluid flow. As shown in Figure 8, at the beginning of blowing (0.1 s), the liquid is blown toward the edge of the molten bath by the top blowing gas. Then, the liquid converges to the center of the molten bath (0.2 s). When the blowing reaches 6 s, the shape of the cavity becomes a semi-steady state. Additionally, it is observed that the velocity at the surface of the molten bath is higher than that of the bottom. As shown in Figure 9, the inverted conical plume formed by bottom-blown gas becomes less obvious due to the effect of the top-blown gas. In addition, due to the flow of bottom blowing gas, the area of the low-velocity zone at the bottom of the molten bath is reduced.

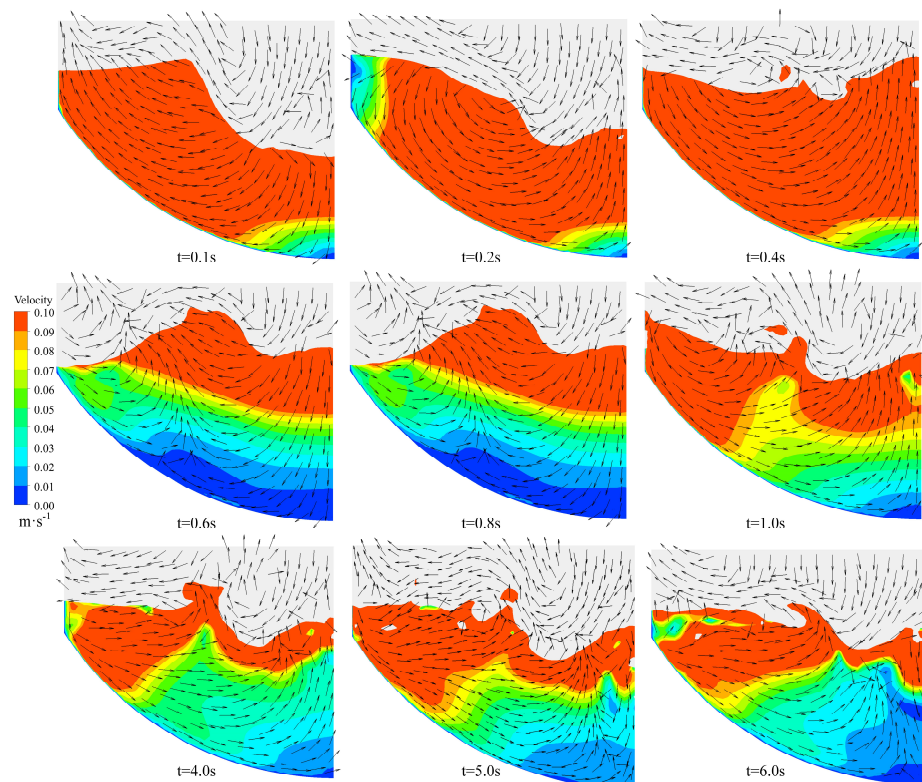


Figure 8. Evolution of flow field in the longitudinal section of the molten bath (top blowing).

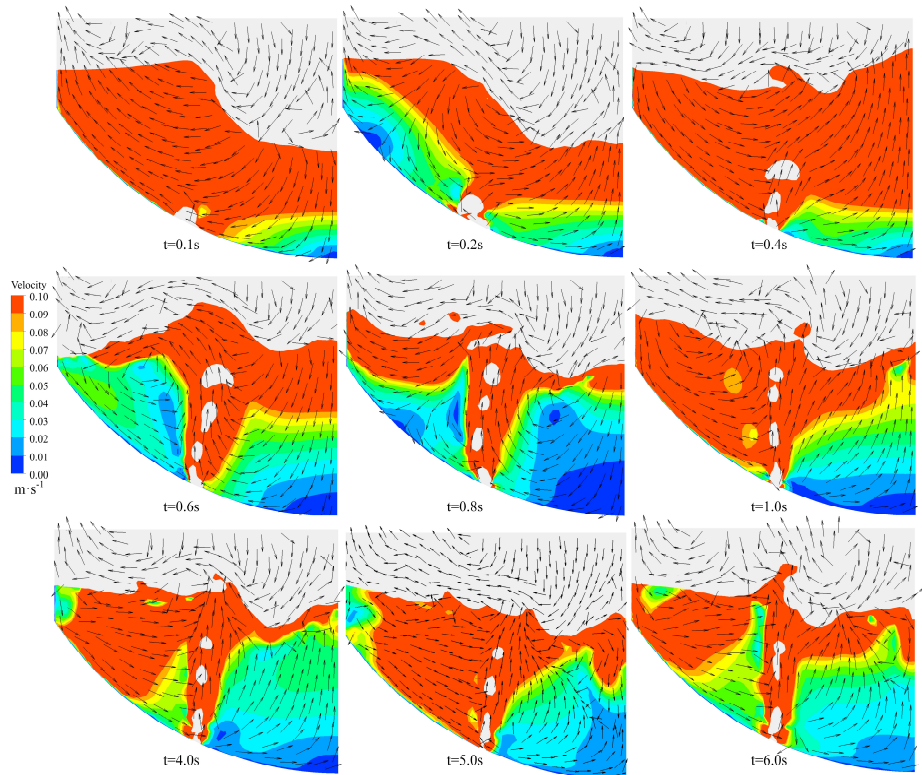


Figure 9. Evolution of flow field in the longitudinal section of the molten bath (combined blowing).

Figure 10 shows the effect of the top blowing flow rate and lance height on the impact cavity shape. It can be seen from Figure 10a that, similar to the reduction in lance height or

rise of the top blowing flow rate, the depth of the cavity increases. In the case where the top blow flow rate is $203.38 \text{ m}^3/\text{h}$, $221.87 \text{ m}^3/\text{h}$, and $240.36 \text{ m}^3/\text{h}$, when the lance height is reduced from 0.400 m to 0.266 m , the cavity depth increases by 163.33% , 78.39% , and 53.33% , respectively. In the three lance heights studied in this article, when the top blowing flow rate increased from $203.38 \text{ m}^3/\text{h}$ to $240.36 \text{ m}^3/\text{h}$, the cavity depth increased by 45.57% , 60.98% , and 150.00% , respectively.

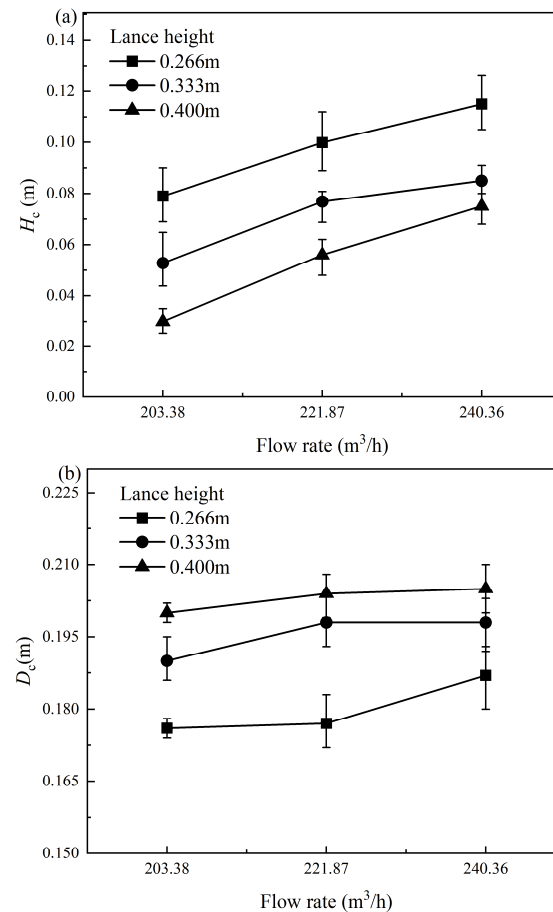


Figure 10. Effects of different top lance heights and flow rates on the cavity shape ((a) the depth of the cavity, (b) the cavity diameter).

In Figure 10b, the increase in the top blowing flow rate and the increase in lance height are beneficial to increasing the cavity diameter. Additionally, it should be noted that the lance height has a much greater impact on the cavity shape than the top blowing flow rate. In the three lance heights studied in this article, when the top blowing flow rate is increased from $203.38 \text{ m}^3/\text{h}$ to $240.36 \text{ m}^3/\text{h}$, the cavity diameter increases by 6.25% , 4.21% , and 2.50% , respectively. In the case of the three flow rates, when the lance height is lifted from 0.266 m to 0.400 m , the cavity diameter increases by 13.63% , 15.25% , and 9.62% , respectively.

4.2. Comparison of Bottom, Top, and Combined Blowing

To study the effects of bottom blowing, top blowing, and combined blowing on the flow of a molten bath, the flow fields of the three under the same conditions were analyzed in Figure 11. It is obvious that the area of the low-velocity zone is the smallest in the case of combined blowing. Moreover, in the bottom blowing converter, the area with a velocity greater than 0.09 m/s is only distributed in the rising inverted conical plume. For the top blowing converter, the area with a larger velocity is distributed on the surface of the molten bath. The combined blowing converter combines the top blow and bottom blow so that the higher velocity area of the molten bath is increased. In other words, a molten bath in

a combined blowing converter is more active than in a top blowing or bottom blowing converter.

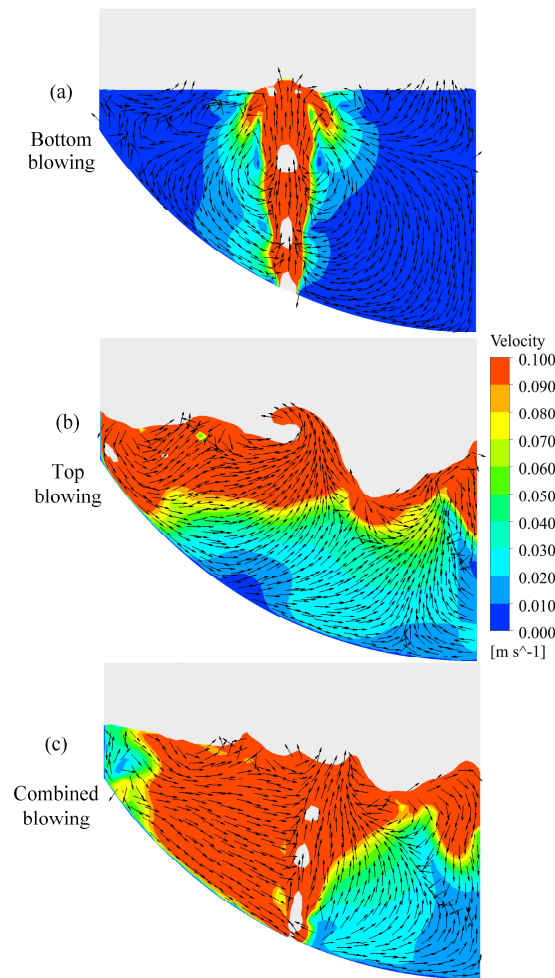


Figure 11. Comparison of the flow fields of the bottom, the top, and the combined blowing converters (longitudinal section).

Further, to study the influence of different operating conditions on the flow of the molten bath cross-section, 10 horizontal planes were taken from different heights, as shown in Figure 12.

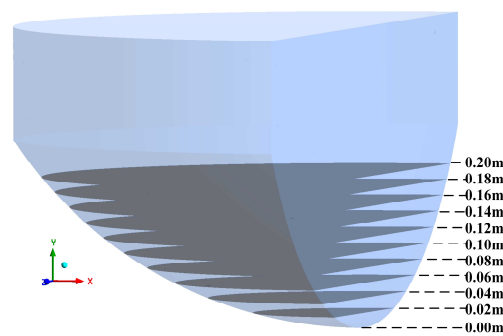


Figure 12. Position of the horizontal planes.

As shown in Figure 13, the flow fields at the bottom, middle, and top of the molten bath were selected to compare the three conditions. It is obvious that, at the bottom of

the molten bath (0.02 m), the flow rate of the combined blowing converter is significantly greater than that of the top blowing and bottom blowing converters. Additionally, the area with a higher velocity in the bottom blow cross-section is only near the bottom tuyeres.

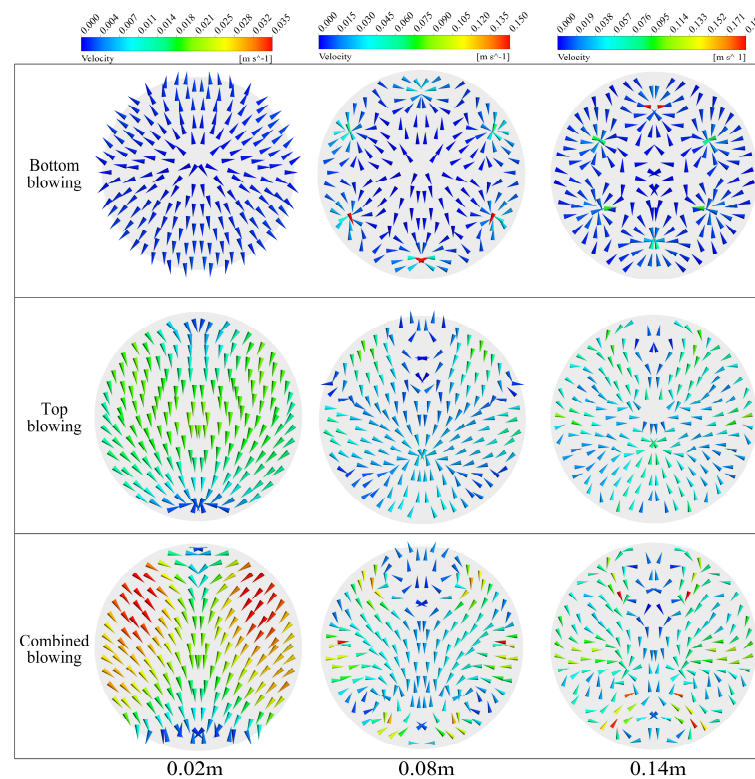


Figure 13. Comparison of the flow fields of the bottom, the top, and the combined blowing converters (horizontal section).

Figure 14 shows a comparison of the radial velocity distribution of different molten bath depths under bottom, top, and combined blowing converters. R is used to represent the distance from the center point of the molten bath. Since the bottom of the converter is hemispherical, the maximum R value is different on each horizontal plane. It can be seen that the velocity of the bottom blowing converter is much lower than that of the top and combined blowing converters. Additionally, it can be seen that the velocity in the center of the molten bath is lower. At a position close to the surface of the molten bath, as shown in Figure 14c,d, compared with top blowing, combined blowing is beneficial to increasing the velocity near the center of the molten bath. It should be pointed out that, in the case of combined blowing, the velocity near the radial distance of 0.23 m increases significantly due to the flow of the bottom blowing gas.

When the bottom blowing flow rate changes in the combined blowing converter, the quantified area-averaged velocity distribution of the molten bath is shown in Figure 15. It is obvious that the velocity of the molten bath is the lowest in the bottom blowing converter. When the height of the horizontal plane reaches 0.06 m, the velocity change of the molten bath becomes very small. In the top blow converter, as the horizontal plane height of the molten bath increases, the velocity shows a continuous increase. In addition, a comparison of the three combined converters is also shown in the figure. Among the three combined blowing converters, the top blowing flow rates are the same, while the bottom blowing flow rates are 1.96 m³/h, 3.92 m³/h, and 5.88 m³/h, respectively. It can be concluded that increasing the bottom blowing flow rate can increase the velocity of each cross-section in the combined blowing converter.

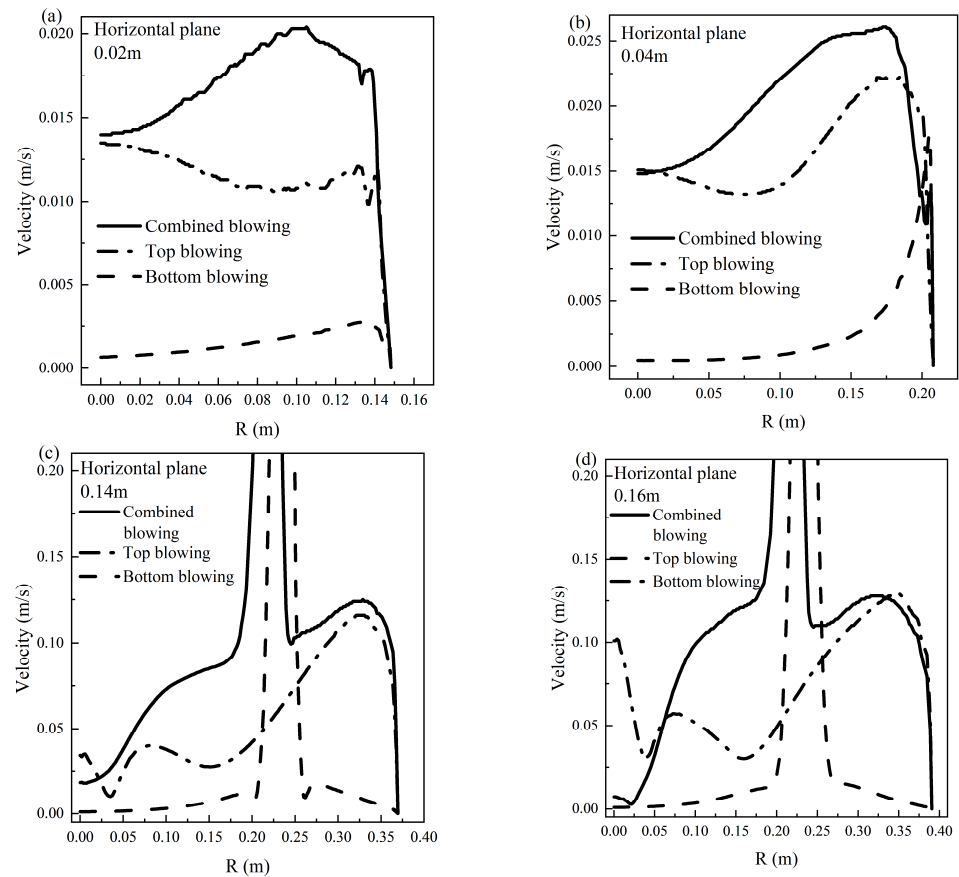


Figure 14. Comparison of the velocity distribution in the radial direction ((a) $Y = 0.02$ m, (b) $Y = 0.04$ m, (c) $Y = 0.14$ m, (d) $Y = 0.16$ m).

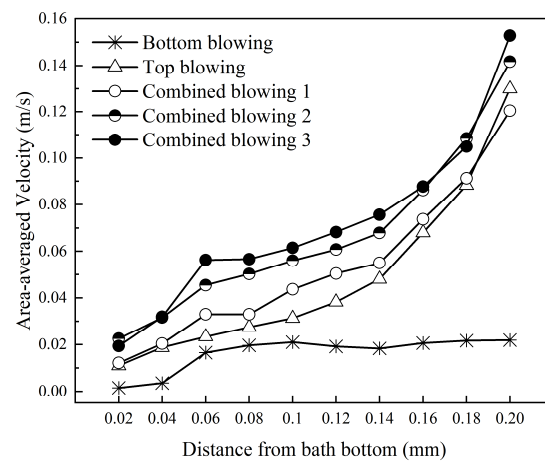


Figure 15. Area-averaged velocity on the horizontal planes of different distances from the bath bottom.

The variation in the percentage increased in velocity across each horizontal plane of the molten bath in the combined blowing converter relative to the top blowing converter is shown in Figure 16. It is observed that, as the distance from the bottom of the molten bath increases, the increased percentage of the area-averaged velocity first increases and then decreases. The greater the bottom blow flow rate, the greater the change in the molten bath velocity. Furthermore, the effect of bottom blowing near the top of the molten bath is very low, and the improvement is less than 10%. This is because top blowing has a great

influence on the liquid state at the top of the molten bath while weakening the influence of the bottom blowing gas.

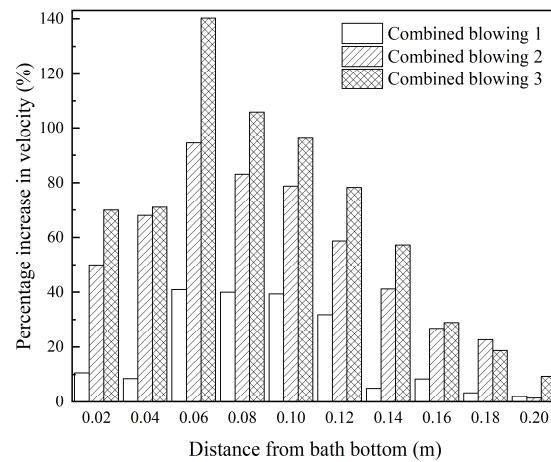


Figure 16. The increased velocity percentages of different combined blowing.

4.3. Effect of the Oxygen Flow Rate on the Bath Flow

Figure 17 shows the radial distribution of the molten bath velocity at different heights of the bath bottom under the condition that the lance height of the top blowing converter is 0.333 m. It can be seen from Figure 17a that the flow velocity at the bottom of the molten bath is the largest when the top blowing flow rate is 221.87 m³/h. Increasing or decreasing the top blow flow can reduce the velocity of the bottom. At a depth of 0.04 m, a lower top blowing flow rate is beneficial to increasing the velocity. At a position close to the molten bath surface, as shown in Figure 17c,d, the high top blow flow rate results in a higher velocity.

Figure 18 shows the velocity at different depths under the combined condition. Similar to the case of the top blowing converter, the flow velocity near the bottom of the molten bath is the largest when the top blowing flow rate is 221.87 m³/h. Compared to top blowing, when the top blowing flow rate changes, the combined blowing converter can make the velocity change at the top of the molten bath smaller, which can be seen from Figure 18c,d.

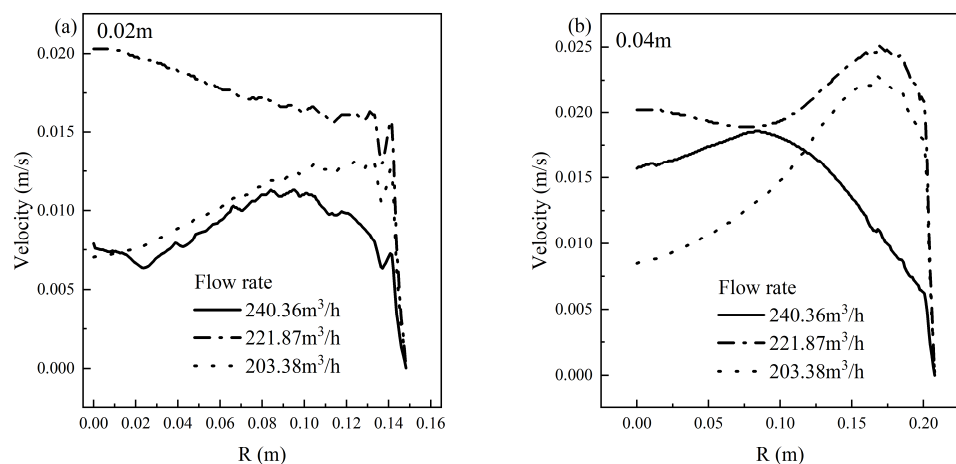


Figure 17. Cont.

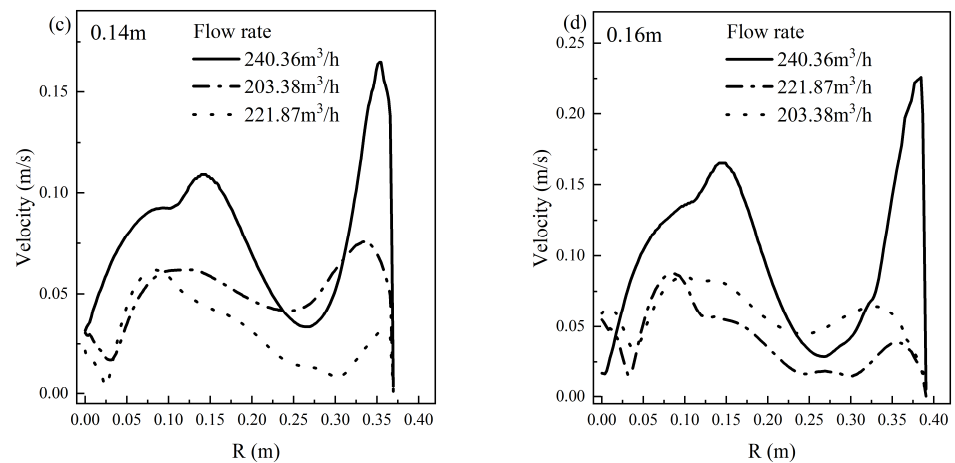


Figure 17. Variation of the radial velocity with the top blow flow rate and molten bath depth (top blowing), (a) $Y = 0.02$ m, (b) $Y = 0.04$ m, (c) $Y = 0.14$ m, (d) $Y = 0.16$ m.

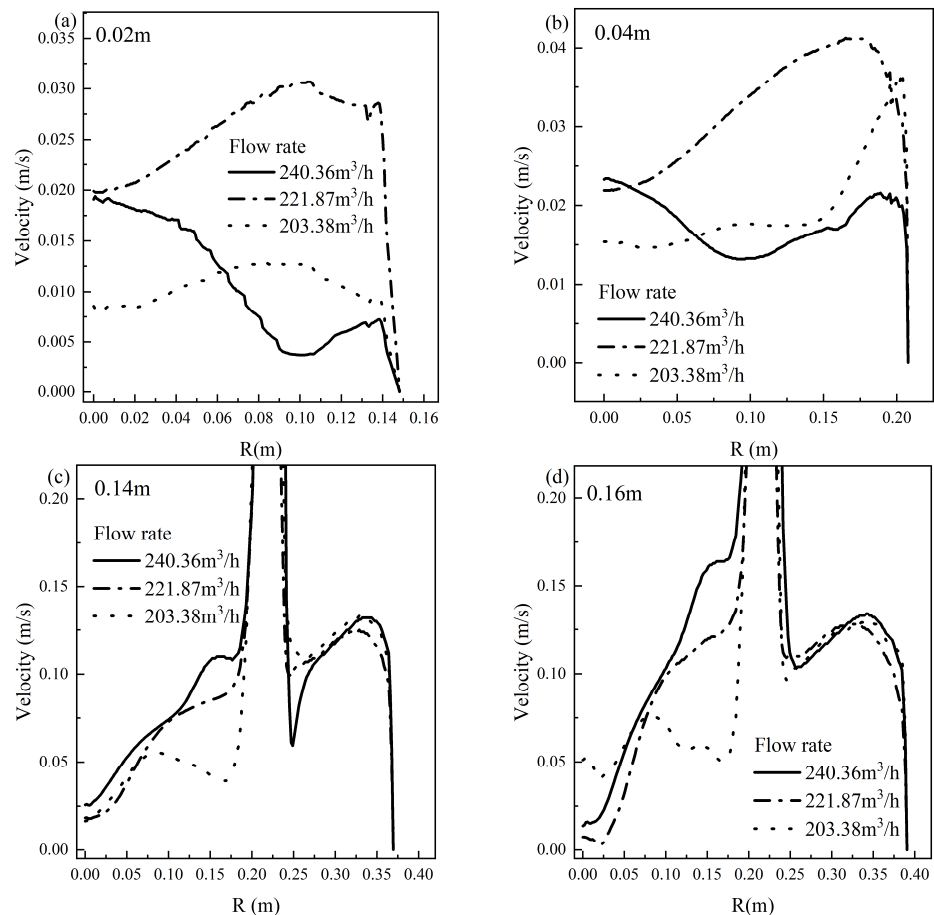


Figure 18. Variation of the radial velocity with the top blow flow rate and molten bath depth (combined blowing), (a) $Y = 0.02$ m, (b) $Y = 0.04$ m, (c) $Y = 0.14$ m, (d) $Y = 0.16$ m.

4.4. Effect of Lance Height on the Bath Flow

In actual production, a higher lance height is used when blowing starts. During the blowing process, the lance height is dynamically adjusted according to the slag conditions to satisfy the decarburization and dephosphorization tasks. At the end of the blowing, the

carbon–oxygen reaction is weak, and a low lance height is used to enhance the fluidity of the molten bath.

In the top blowing converter, the radial velocities near the bottom and top of the molten bath at different lance heights are shown in Figure 19. It can be seen from Figure 19a,b that, at a low lance height, the velocity of the liquid steel on the lower part of the bath is higher. In other words, a low lance height can promote the flow at the bottom of the molten bath. Moreover, the lance height has a relatively small impact on the velocity near the edge of the molten bath. For the upper part of the molten bath, in Figure 19c,d, the velocity distribution appears to be significantly different. When the radial distance is less than 0.2 m, a lower lance height is still beneficial to increasing the liquid velocity. In the range of radial distances greater than 0.2 m, the lance height is 0.400 m, which makes the liquid velocity much higher. Additionally, under the condition of the same lance height, the higher the height of the cross-section of the molten bath, the greater the maximum velocity.

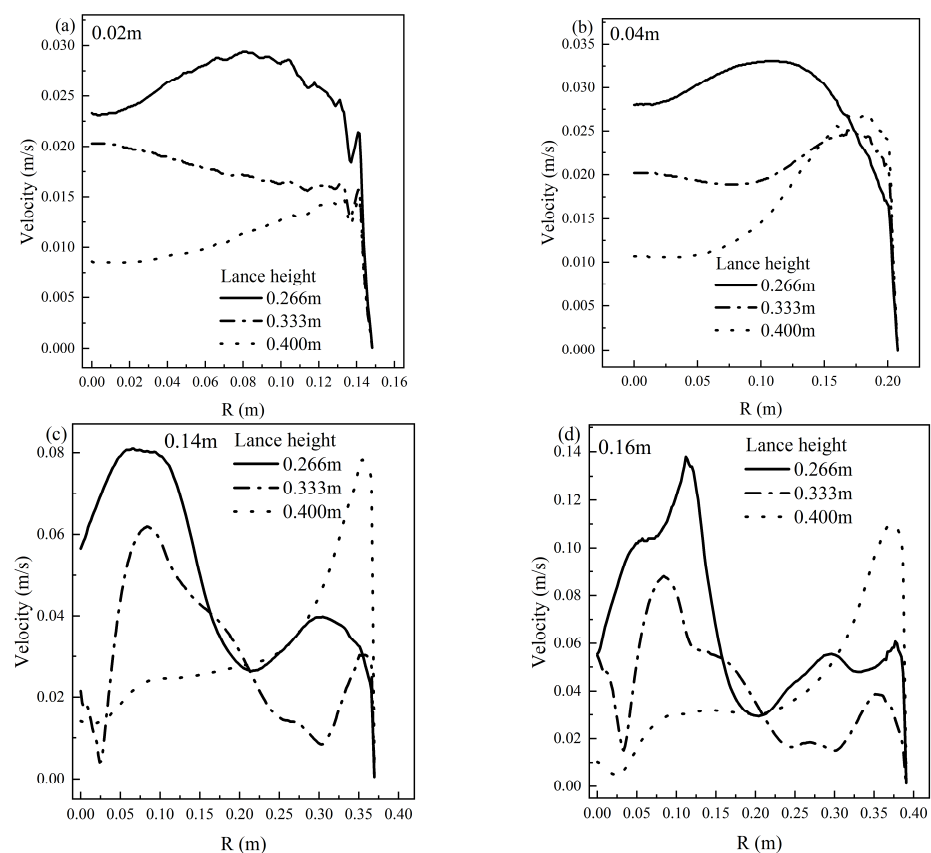


Figure 19. Velocity distribution in the radial direction at different depths of the molten bath (top blowing, (a) $Y = 0.02$ m, (b) $Y = 0.04$ m, (c) $Y = 0.14$ m, (d) $Y = 0.16$ m).

Figure 20 gives the influence of different lance heights on the molten bath velocity in the combined blowing condition. It can be seen from Figure 20a,b that, at the bottom of the molten bath, a lower lance height is beneficial to increasing the liquid velocity, which is the same as the top blowing converter. This is because the liquid at the bottom is less affected by the bottom blow. Figure 20c,d depicts that, when approaching the molten bath surface, a lance height of 0.333 m is more conducive to increasing the velocity. When the lance height is 0.266 m and 0.400 m, respectively, the radial velocity distribution is similar.

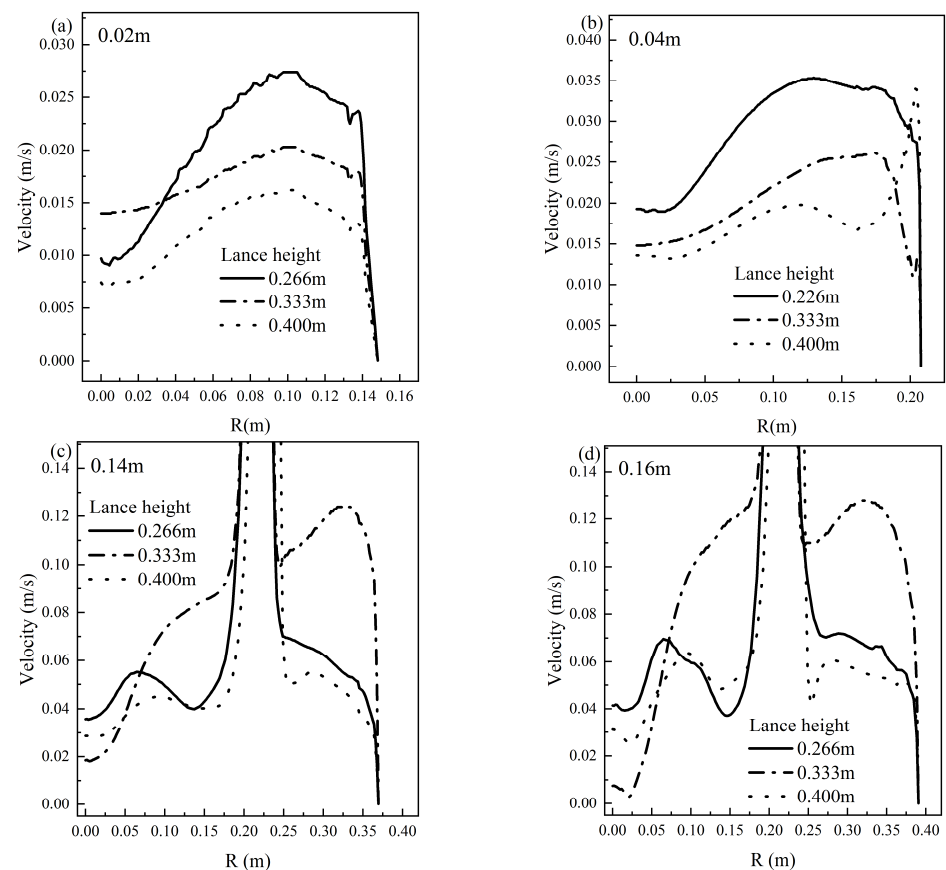


Figure 20. Velocity distribution in the radial direction at different depths of the molten bath (combined blowing, (a) $Y = 0.02$ m, (b) $Y = 0.04$ m, (c) $Y = 0.14$ m, (d) $Y = 0.16$ m).

4.5. The “Inactive Zone” Analysis

The volume ratio of the “inactive zone” to bath volume is calculated to compare the bath flow with different operations. The “inactive zone” is defined as the region where the velocity flow is lower than 0.01 m/s in the bath.

Figure 21 illustrates the comparison of “inactive zone” ratios for the bottom, top, and combined blowing converters. As shown in the results, the ratio in the bottom blow converter reaches about 63%, while the top blow converter reduces a ratio less than 3%. This indicates that there is a significant difference in the “inactive zone” volume between the top blow and bottom blow. Meanwhile, the combined blowing converter further reduced this ratio. When the bottom blow flow rate during the combined process increased from 1.96 m³/h to 5.88 m³/h, this ratio decreased by 0.72%.

Figure 22 gives the “inactive zone” ratio in the bath of the bottom blowing converter. When the bottom flow rate increased by more than three times, the ratio only decreased by 17%.

Figure 23 shows the “inactive zone” ratio of the top blowing converters with different top lance heights and top blowing flow rates. As shown in the figure, increasing the top blow flow rate can only slightly reduce the ratio when the lance height is the same. The decrease in the lance height significantly reduces the ratio. For instance, when the flow rate is 203.38 m³/h, the lance lifts from 0.400 m to 0.333 m and 0.266 m, and the ratio decreases from 1.92% to 1.26%, then to 0.26%, respectively.

Figure 24 shows the variation in the “inactive zone” ratio in the combined blowing converter. By comparing with the top blowing, it can be seen that the ratio of the combined blowing converter is lower. When the top blow flow rate is the same, lowering the lance height can reduce this ratio. It should be noted that, when the lance height is 0.266 m, the change in the flow rate has little effect on this ratio. When the lance height is 0.333 m and

0.400 m, as the top blow flow rate increases, the ratio first increases and then decreases. It should be pointed out that the change of the “inactive zone” ratio caused by the change in lance height or top blowing flow rate is less than 1%.

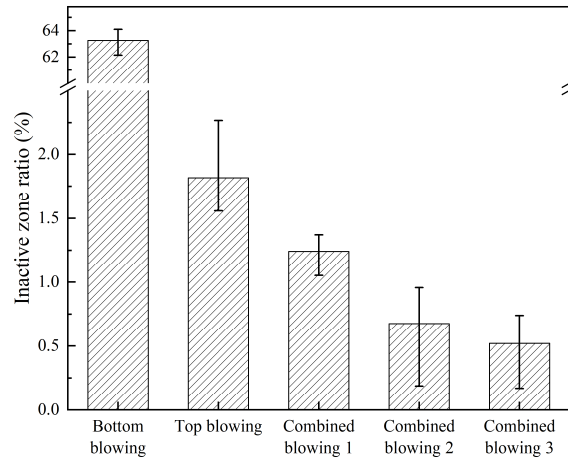


Figure 21. The “inactive zone” ratio in the bath of the top and bottom blowing converters.

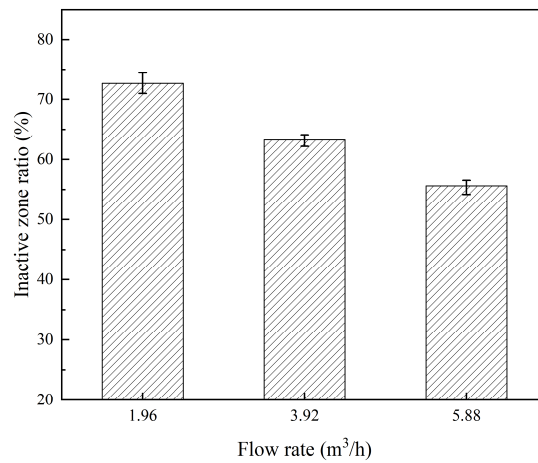


Figure 22. The “inactive zone” ratio in the bath of the bottom blowing converter.

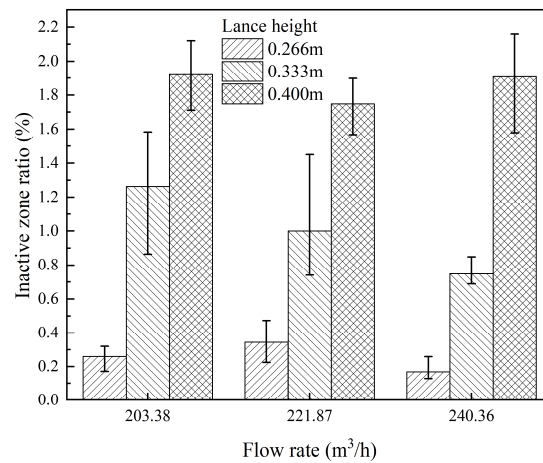


Figure 23. The “inactive zone” ratio in the bath of the top blowing converter.

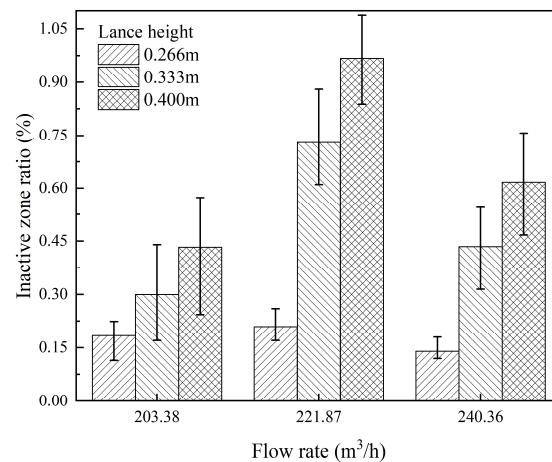


Figure 24. The “inactive zone” ratio in the bath of the combined blowing converter.

The findings of this study have to be viewed in light of some limitations. The thickness, density, and viscosity of the slag during the blowing process are in a state of change, and there are significant differences between the early and end stages of blowing. The properties of the slag may affect the impact of the oxygen jet on the molten bath. In addition, the degree of carbon–oxygen reaction in the molten bath also has a great influence on the mixing of the molten bath. In future works, we plan to study the influence of the slag and carbon–oxygen reaction in different blowing stages on the flow of molten baths. Further, the research results can provide a reference for the designation of the lance height and top blowing flow rate at different stages of blowing.

5. Conclusions

In this article, the flow of a molten bath in the combined blowing process of a 1/6 reduced scale model based on a 210 t converter was studied using Fluent 2022R1. In the model, water, oil, and air were used to represent liquid steel, liquid slag, and argon, respectively. The velocity distribution and “inactive zone” ratio in bottom blowing, top blowing, and combined blowing converters were also compared. The conclusions from this work are summarized as follows.

(1) A fully developed cavity could be obtained about 6 s after blowing. The measured values of the cavity of the physical model were close to the simulation results.

(2) In the bottom blowing converter, the area with a velocity greater than 0.09 m/s was only distributed in the rising inverted conical plume. For the top blowing converter, the area with a velocity greater than 0.09 m/s was distributed on the surface of the molten bath. The combined blowing converter combined the top blow and bottom blow so that the higher velocity area of the molten bath was increased.

(3) Compared with the top blowing converter, the increased percentage of the area-averaged velocity in the combined blowing converter first increased and then decreased as the distance from the bottom increased. The effect of bottom blowing near the top of the molten bath was very low, and the improvement was less than 10%.

(4) A low lance height could promote the flow at the bottom of the molten bath. When the top blowing flow rate changed, the combined blowing converter made the velocity change at the top of the molten bath smaller.

(5) In the top blowing converter, the decrease in the lance height significantly reduced the “inactive zone” ratio, while the changes in the top blowing flow rate had less impact. When the flow rate was 203.38 m³/h, the lance height lifted from 0.400 m to 0.333 m and 0.266 m, and the ratio decreased from 1.92% to 1.26%, then to 0.26%, respectively. In the combined blowing converter, the change in the lance height or the top blowing flow rate was less than 1%.

Author Contributions: Conceptualization, Z.L. and S.C.; methodology, J.P.; software, Z.L. and J.P.; validation, Z.L.; formal analysis, Z.L.; investigation, Z.L. and J.P.; resources, S.C.; data curation, Z.L. and J.P.; writing—original draft preparation, Z.L.; writing—review and editing, Z.L. and S.C.; visualization, Z.L. and S.C.; supervision, S.C.; project administration, S.C.; funding acquisition, S.C. All authors have read and agreed to the published version of the manuscript.

Funding: This research was funded by the National Natural Science Foundation of China, grant number 62071034.

Data Availability Statement: The data presented in this study are available on request from the corresponding author. The data are not publicly available due to the fund's policy or confidentiality agreement.

Conflicts of Interest: The authors declare no conflicts of interest.

Nomenclature

α_i	ith volume fraction (-)
ρ_i	density of the ith volume fraction ($\text{kg}\cdot\text{m}^{-3}$)
p	pressure (MPa)
R	gas constant = $8.314 \text{ J}\cdot\text{mol}^{-1}\cdot\text{K}^{-1}$
T	temperature (K)
μ	average viscosity of the volume fraction ($\text{kg}\cdot\text{m}^{-1}\cdot\text{s}^{-1}$)
\vec{v}	the instantaneous velocity of the phase ($\text{m}\cdot\text{s}^{-1}$)
\vec{g}	gravity acceleration ($\text{m}\cdot\text{s}^{-2}$)
\vec{F}	volume force ($\text{kg}\cdot\text{m}^{-2}\cdot\text{s}^{-2}$)
E	energy (J)
λ_{eff}	effective thermal conductivity ($\text{W}\cdot\text{m}^{-1}\cdot\text{K}^{-1}$)
Sh	the volumetric heat sources ($\text{W}\cdot\text{m}^{-1}$)

References

1. Szekely, J.; Asai, S. Turbulent fluid flow phenomena in metals processing operations: Mathematical description of the fluid flow field in a bath caused by an impinging gas jet. *Metall. Mater. Trans. B* **1974**, *5*, 463–467. [\[CrossRef\]](#)
2. Alam, M.; Naser, J.; Brooks, G.; Fontana, A. A computational fluid dynamics model of shrouded supersonic jet impingement on a water surface. *ISIJ Int.* **2012**, *52*, 1026–1035. [\[CrossRef\]](#)
3. Lv, M.; Zhu, R.; Guo, Y.G.; Wang, Y.W. Simulation of flow fluid in the BOF steelmaking process. *Metall. Mater. Trans. B* **2013**, *44*, 1560–1571. [\[CrossRef\]](#)
4. Li, Q.; Li, M.; Kuang, S.B.; Zou, Z. Computational study on the behaviours of supersonic jets and their impingement onto molten liquid free surface in BOF steelmaking. *Can. Metall. Q.* **2014**, *53*, 340–351. [\[CrossRef\]](#)
5. Zhou, X.; Ersson, M.; Zhong, L.; Yu, J.; Jönsson, P. Mathematical and physical simulation of a top blown converter. *Steel Res. Int.* **2014**, *85*, 273–281. [\[CrossRef\]](#)
6. Li, Q.; Li, M.; Kuang, S.; Zou, Z. Numerical simulation of the interaction between supersonic oxygen jets and molten slag-metal bath in steelmaking BOF process. *Metall. Mater. Trans. B* **2015**, *46*, 1494–1509. [\[CrossRef\]](#)
7. Zhou, X.; Ersson, M.; Zhong, L.; Jönsson, P. Numerical simulations of the kinetic energy transfer in the bath of a BOF converter. *Metall. Mater. Trans. B* **2016**, *47*, 434–445. [\[CrossRef\]](#)
8. Liu, G.Q.; Li, J.N.; Xu, D.; Zheng, B. Energy balance between multiple supersonic jets and molten bath in BOF steelmaking. *Ironmak. Steelmak.* **2022**, *49*, 726–736. [\[CrossRef\]](#)
9. Li, M.; Li, Q.; Kuang, S.; Zou, Z. Transferring characteristics of momentum/energy during oxygen jetting into the molten bath in BOFs: A computational exploration. *Steel Res. Int.* **2016**, *87*, 288–300. [\[CrossRef\]](#)
10. Zhou, X.; Liu, Y.; Ni, P.; Peng, S. Toward the Bath Flow Interaction of a 250 t Combined Top and Bottom Blowing Converter Based on a Mathematical Modeling. *Steel Res. Int.* **2021**, *92*, 2000334. [\[CrossRef\]](#)
11. Ajmani, S.K.; Chatterjee, A. Cold model studies of mixing and mass transfer in steelmaking vessels. *Ironmak. Steelmak.* **2005**, *32*, 515–527. [\[CrossRef\]](#)
12. Liu, G.; Liu, K.; Han, P.; Chen, Y. Numerical investigation on behaviors of interlaced jets and their interaction with bath in BOF steelmaking. *AIP Adv.* **2019**, *9*, 075202. [\[CrossRef\]](#)
13. Li, M.; Li, Q.; Kuang, S.; Zou, Z. Determination of cavity dimensions induced by impingement of gas jets onto a liquid bath. *Mater. Trans. B* **2016**, *47*, 116–126. [\[CrossRef\]](#)
14. Amano, S.; Sato, S.; Takahashi, Y.; Kikuchi, N. Effect of top and bottom blowing conditions on spitting in converter. *Eng. Rep.* **2021**, *3*, e12406. [\[CrossRef\]](#)

15. Sun, J.; Zhang, J.; Lin, W.; Cao, L.; Feng, X.; Liu, Q. Effect of impact cavity shape induced by supersonic oxygen jet on the dynamic characteristics of molten bath in converter. *Steel Res. Int.* **2021**, *92*, 2100179. [[CrossRef](#)]
16. Sun, J.; Zhang, J.; Lin, W.; Feng, X.; Liu, Q. Effect of bottom blowing mode on fluid flow and mixing behavior in converter. *Metals* **2022**, *12*, 117. [[CrossRef](#)]
17. Sun, J.; Zhang, J.; Jiang, R.; Feng, X.; Liu, Q. Effect of Bottom Tuyere Arrangement Based on Impact Cavity Morphology on Kinetic Behavior of Molten Bath in Converter. *Steel Res. Int.* **2023**, *94*, 2200532. [[CrossRef](#)]
18. Qi, F.; Zhou, S.; Zhang, L.; Liu, Z.; Cheung, S.C.; Li, B. Numerical Study on Interfacial Structure and Mixing Characteristics in Converter Based on CLSVOF Method. *Metals* **2023**, *13*, 880. [[CrossRef](#)]
19. Zhang, J.; Lou, W.; Shao, P.; Zhu, M. Mathematical Simulation of Impact Cavity and Gas-Liquid Two-Phase Flow in Top-Bottom Blown Converter with Eulerian-Multifluid VOF Model. *Mater. Trans. B* **2022**, *53*, 3585–3601. [[CrossRef](#)]
20. Ajmani, S.K.; Chatterjee, A. Cold model study of mixing and mass transfer in LD converters at Tata Steel. *Ironmak. Steelmak.* **1996**, *23*, 335–345.
21. Olivares, O.; Elias, A.; Sanchez, R.; Díaz-Cruz, M.; Morales, R.D. Physical and mathematical models of gas-liquid fluid dynamics in LD converters. *Steel Res. Int.* **2002**, *73*, 44–51. [[CrossRef](#)]
22. Amini, Y.; Ghazanfari, V.; Heydari, M.; Shadman, M.M.; Khamseh, A.G.; Khani, M.H.; Hassanvand, A. Computational fluid dynamics simulation of two-phase flow patterns in a serpentine microfluidic device. *Sci. Rep.* **2023**, *13*, 9483. [[CrossRef](#)] [[PubMed](#)]
23. Launder, B.E.; Spalding, D.B. *Mathematical Models of Turbulence*, 1st ed.; Academic Press: London, UK, 1972; pp. 124–130.
24. Zore, K.; Sasanapuri, B.; Parkhi, G.; Varghese, A. Ansys mosaic poly-hexcore mesh for high-lift aircraft configuration. In Proceedings of the 21th Annual CFD Symposium, Bangalore, India, 8–9 August 2019; pp. 1–11.

Disclaimer/Publisher’s Note: The statements, opinions and data contained in all publications are solely those of the individual author(s) and contributor(s) and not of MDPI and/or the editor(s). MDPI and/or the editor(s) disclaim responsibility for any injury to people or property resulting from any ideas, methods, instructions or products referred to in the content.